https://doi.org/10.5194/egusphere-2025-6017
Preprint. Discussion started: 21 January 2026

Process-based evaluation of ENSO simulation sensitivity to horizontal resolution in the Chinese Academy of Sciences FGOALS-f3 Climate System Model

Meng-Er Song[1], Lin Chen[1], Yongqiang Yu[2], Bo An[2], Jiuwei Zhao[1], Hai Zhi[1]

[1] State Key Laboratory of Climate System Prediction and Risk Management/Key Laboratory of Meteorological Disaster, Ministry of Education/Collaborative Innovation Center on Forecast and Evaluation of Meteorological Disasters, Nanjing University of Information Science and Technology, Nanjing 210044

[2] State Key Laboratory of Earth System Numerical Modeling and Application, Institute of Atmospheric Physics, Chinese Academy of Sciences, Beijing, China

Correspondence to: Lin Chen (chenlin@nuist.edu.cn)

Abstract. El Niño-Southern Oscillation (ENSO) is the most prominent interannual climate variability, hence its simulation performance represents a critical benchmark for evaluating the fidelity of coupled climate models. Increasing model resolution is an effective approach to improve the model simulation; however, the impact of refining horizontal resolution from the hundred-kilometer scale to the tens-of-kilometer scale on ENSO simulation, as well as the underlying mechanisms, remains unclear. This study provides a process-based evaluation of ENSO behaviour in two versions of the Chinese Academy of Sciences Flexible Global Ocean–Atmosphere–Land System Finite-Volume version 3 (FGOALS-f3) climate system model: a low-resolution configuration (~100 km; FGOALS-f3-L, hereafter f3-L) and a high-resolution configuration (~25 km; FGOALS-f3-H, hereafter f3-H). Using a reproducible diagnostic framework, we assess how horizontal resolution influences ENSO amplitude, oscillation characteristics, key air–sea coupling processes, and high-frequency (HF) atmospheric variability. The low-resolution severely overestimates ENSO amplitude, whereas f3-H produces amplitude closer to the observation. Process-based diagnostics show that this improvement arises from the more realistic representation of thermocline and zonal advection feedback processes in f3-H, which arises from the more realistic representation of the meridional structure of ENSO-related zonal wind stress anomalies over equatorial Pacific in f3-H and can be traced back to its improved horizontal resolution. The ENSO cycle in f3-L exhibits excessive regularity, featuring periodic warm-cold transitions; while f3-H reproduces an irregular oscillation resembling the observation. The excessive regularity in f3-L is attributed to its coarser resolution, which limits the simulation performance of tropical cyclones and consequently weakens high-frequency westerly wind activity over the tropical Pacific. The feeble stochastic forcing in f3-L is insufficient to disrupt its overly intense ENSO cycle, yielding an overly regular oscillation. By identifying the structural sources of ENSO biases across resolutions, this study provides a reproducible and model-agnostic framework for diagnosing resolution effects on ENSO performance in climate models and informs future development of FGOALS-f3 model family.

1 Introduction

El Niño-Southern Oscillation (ENSO), as one of the most prominent interannual variabilities in the Earth's climate system, exerts a profound influence on regional and global climate (McPhaden et al., 2006; Cai et al., 2021). Therefore, the ability to accurately simulate ENSO phenomenon serves as a fundamental benchmark for evaluating the fidelity of coupled climate models (Timmermann et al., 2018). Despite significant progress in the development of climate models, large inter-model spread remains in ENSO characteristics across Coupled Model Intercomparison Project (CMIP) generations (Zhang et al., 2020; Planton et al., 2021). Common biases include inaccuracies in simulating ENSO amplitude (Planton et al., 2021), period (Lu et al., 2018), seasonal phase locking (Liao et al., 2023; Yan and Sun, 2024), spatial distribution (Jiang et al., 2021), and intensity asymmetry (Zhao and Sun, 2022), as well as overly regular ENSO oscillation (Chen et al., 2016; Guilyardi et al., 2020). These deficiencies reflect systematic structural biases within models, which directly limit the predictive skill of dynamical models (Barnston et al., 2012) and hinder the reliability of climate projection regarding how ENSO may evolve under future climate change (Jiang et al., 2020a). Therefore, it is imperative to improve the fidelity of ENSO simulation in climate models.

Horizontal resolution has long been recognized as an important factor influencing model behavior (Yu et al., 2024). Motivated by this, the latest CMIP6 launched a dedicated High-Resolution Model Inter-comparison Project (HighResMIP) (Eyring et al., 2016) to systematically assess the benefits of increased resolution on model simulations. Previous studies have shown that as model resolution increases, simulation capabilities for both the climate mean state and variability exhibit improvements (Dawson et al., 2013; Chang et al., 2020). For example, high-resolution models demonstrate superior performance over low-resolution counterparts in simulating the Asian summer monsoon (He et al., 2025a), the impact of Tibetan Plateau thermal forcing on Asian summer monsoon (He et al., 2025b), the precipitation in southern China (Zi et al., 2024), the spatial distribution and frequency of tropical cyclones (Kreussler et al., 2021; Li et al., 2021), air-sea turbulent flux (Small et al., 2019), heat transport by boundary currents (Docquier et al., 2019), ocean mesoscale eddies (Hallberg, 2013), and Antarctic sea ice (Docquier et al., 2019). This is partly because higher resolution allows models to explicitly resolve finer-scale physical processes, reducing their dependence on parameterization schemes. Furthermore, high-resolution models facilitate a more accurate simulation of topographically sensitive regions, therefore improving the simulation of atmosphere-ocean processes related to complex terrain (Bacmeister et al., 2014; Hewitt et al., 2016). Then a pertinent inquiry arises: does the ENSO simulation benefit from the increased resolution?

Regarding the impact of increased horizontal resolution on ENSO characteristics, previous studies found that when the atmospheric horizontal resolution in climate models was increased from 3.8° (T30) or 2.8° (T42) to 1° (T106), significant improvements can be found in the simulated ENSO period (Guilyardi et al., 2004; Navarra et al., 2008) and ENSO amplitude (Hua et al., 2018). However, the aforementioned studies were primarily based on the comparisons from ~400 km (or 300 km) to 100 km scales. In the latest climate models participated in the HighResMIP, model resolutions have advanced substantially, with some achieving 25 km resolution in atmospheric component and 10 km in oceanic component. This higher resolution enables a more realistic reproduction of climate variability, such as tropical cyclones (TCs) (Li et al., 2021) and tropical instability waves (Li et al., 2023). Yet, a critical question remains unresolved: when model resolution reaches ~25 km, a scale that can reasonably simulate weather-scale systems like TCs, does ENSO simulation also improve further?

ENSO is fundamentally driven by a number of coupled ocean-atmosphere feedbacks (Li, 1997; Jin et al., 2006; Chen et al., 2015b; Chen et al., 2016); however, some analyses regarding ENSO simulations are often result-oriented, focusing only on changes in statistical indices while lacking sufficient diagnostic analysis of the key air-sea feedback processes that shape ENSO's properties. Therefore, it is necessary to conduct a process-oriented evaluation when comparing the ENSO simulation between different resolution versions.

It is worth noting that the observational evidences have suggested the significant influence of atmospheric "noise" on the development and evolution of ENSO (Chen et al., 2015a; Fedorov et al., 2015). Here the atmospheric "noise" primarily refers to high-frequency (HF) wind activities such as westerly wind bursts (Harrison and Vecchi, 1997; Fedorov, 2002), including synoptic and intra-seasonal scales. TC and Madden-Julian Oscillation (MJO; Madden and Julian, 1971; Madden and Julian, 1972) have been recognized as key sources of HF wind activities in recent studies (Ying et al., 2019; Liang and Fedorov, 2021). Considering the atmospheric components in HighResMIP models can reach a horizontal resolution of 50 km or finer (which is sufficient to reasonably reproduce TC features) and that the simulation performance for TC and MJO activities improves with increasing resolution (Davis, 2018;

Tang et al., 2022; Roberts et al., 2025), a further question arises: does the improved simulation of HF activities like TCs and MJO in high-resolution models contribute to improved ENSO simulation?

Motivated by these open questions, this study will conduct a process-oriented evaluation of ENSO simulation for a Chinese climate model, the Flexible Global Ocean–Atmosphere–Land System Finite-Volume version 3 (FGOALS-f3) climate system model that was developed by the Institute of Atmospheric Physics, Chinese Academy of Sciences (IAP-CAS). FGOALS-f3 participated in HighResMIP with both a low-resolution (~100 km; FGOALS-f3-L, hereafter f3-L) and a high-resolution version (~25 km; FGOALS-f3-H, hereafter f3-H) (An et al., 2022; Bao et al., 2020). The high-resolution version (f3-H) has been shown to have superior simulation performances over the low-resolution counterpart (f3-L) in representing mesoscale vortices (An et al., 2022), tropical instability waves (Li et al., 2023), TCs (Li et al., 2021), East Asian summer monsoon precipitation (Zi et al., 2024), and the climatological mean states (Yu et al., 2024). Therefore, this study employs the CAS-developed f3-H and f3-L to reveal the impact of model resolution on ENSO simulation performance and the underlying air-sea coupling processes.

This model evaluation study will provide insights into the resolution sensitivity of ENSO-related processes in FGOALS-f3 and establishes a diagnostic framework that can be applied to other coupled models participating in CMIP6 and future CMIP phases. The remainder of this paper is organized as follows. Section 2 describes the model configurations, observational datasets, and diagnostic framework. Section 3 presents an overview of the ENSO characteristics in two versions of FGOALS-f3 model. Section 4 and Section 5 demonstrate how the model horizontal resolution impacts the ENSO simulation. Section 6 summarizes the findings and discusses implications for model development and evaluation.

2. Model configurations, datasets, and diagnostic framework

2.1 Model configurations

FGOALS-f3 is a fully coupled climate system model developed by State Key Laboratory of Numerical Modeling for Atmospheric Sciences and Geophysical Fluid Dynamics (LASG), IAP-CAS, which couples four component models using the CPL7 coupler (Craig et al., 2012). The four component models are the atmospheric model FAMIL2.2 (He et al., 2019; Li et al., 2021), the ocean model LICOM3.0 (Li et al., 2020), the land model CLM4.0 (Lawrence et al., 2011), and the sea ice model

CICE4.0 (Hunke and Lipscomb, 2010).

The atmospheric component FAMIL2.2 is the last version of the Finite-volume Atmospheric Model developed by the LASG-IAP (FAMIL) (Li et al., 2021). FAMIL2.2 utilizes a finite-volume dynamical core constructed on a cubed sphere grid that is globally partitioned into six tiles (Zhou et al., 2015). In the vertical direction, the model use hybrid coordinates over 32 layers, and the model top is 1 hPa. While the horizontal resolution ranges from C96 (about 100 km) to C384 (about 25 km) across the different resolution version. The oceanic component LICOM 3.0 is the third version of LASG-IAP Climate System Ocean Model (LICOM) (Yu et al., 2018). LICOM 3.0 updated a new advection scheme and employed a tripolar grid based on orthogonal curvilinear coordinates. The horizontal resolution of LICOM 3.0 can vary flexibly between 1°and 1/20°. Sub-grid parametrization schemes employed in LICOM 3.0 include the tidal mixing scheme, a buoyancy frequency related thickness diffusivity scheme, a vertical viscosity and diffusion scheme, and a chlorophyll-a dependent solar penetration scheme, etc. A comprehensive description of the physical package in LICOM3.0 can be found in Li et al. (2020). The land component in FGOALS-f3 model is Community Land Model (CLM) version 4.0. This advanced model simulates the water and momentum balances at the land surface and incorporates interactive carbon and nitrogen cycles, allowing for a more realistic representation of vegetation dynamics and ecosystem processes (Lawrence et al., 2011). In FGOALS-f3 model, sea ice is simulated using the Los Alamos Sea Ice Model version 4.0 (CICE 4.0). This is a dynamic-thermodynamic model that simulates the evolution of sea ice thickness, concentration, and velocity. It features multiple ice thickness categories and an elastic-viscous-plastic (EVP) rheology to model ice deformation and dynamics (Hunke and Lipscomb, 2010).

The FGOALS-f3 model includes two versions: f3-L and f3-H (He et al., 2019; An et al., 2022). Both models are participating in HighResMIP of CMIP6 and have successfully completed the Tier-1 and Tier-3 experiments. These two models have the same components and physical processes. The sole distinction between f3-H and f3-L lies in their horizontal resolution and the corresponding time steps within their finite-volume cubed-sphere dynamical core (FV3). To maintain the stability of the integration for the dynamical core, the two parameters (k_split and n_split) in FV3 are set to 6 and 15 in f3-H, respectively (they are 2 and 6, respectively, in f3-L). The specific resolutions of each component of f3-L and f3-H models are shown in Table 1.

https://doi.org/10.5194/egusphere-2025-6017
Preprint. Discussion started: 21 January 2026

Table 1. Resolution comparison of each component model between the FGOALS-f3-L model and the FGOALS-f3-H model

	FGOALS-f3-L	FGOALS-f3-H
Atmosphere	FAMIL2.2 (1°×1°, 32 levels)	FAMIL2.2 (0.25°×0.25°, 32 levels)
Ocean	LICOM3.0 (1°×1°, 30 levels)	LICOM3.0 (0.1°×0.1°, 55 levels)
Land	CLIM4.0 (1.25°×0.9°)	CLIM4.0 (0.31°×0.23°)
Sea Ice	CICE4.0 (1°×1°)	CICE4.0 (0.1°×0.1°)

The model data used in this study are obtained from the historical experiment outputs of f3-L and f3-H model. Considering the experiment outputs of f3-H (highresSST-present) start from 1950, the period during 1950-2014 for the two models are analyzed. The main variables used in this study include monthly sea surface temperature (SST), three-dimensional ocean currents (uo, vo, wo), oceanic potential temperature (thetao), surface wind stress (tauu, tauv), and net radiation flux (rsds, rsus, rlds, rlus, hfss, hfls); daily surface wind (uas, vas), precipitation (pr), six-hourly sea level pressure (SLP), 850 hPa wind (ua, va), 300 hPa and 500 hPa temperature (ta). All data is detrended before analyzing.

2.2 Observation and reanalysis datasets

The observational and reanalysis data used in this study include: 1) the monthly SST data obtained from the Hadley Centre Sea Ice and Sea Surface Temperature version 1.1 dataset (HadISST v1,1), with a horizontal resolution of 1°×1° (Rayner et al., 2003); 2) the monthly, daily, and hourly 10m wind fields are from the European Centre for Medium-Range Weather Forecasts (ECMWF) reanalysis data Fifth Generation (ERA5), with a horizontal resolution of 0.25°× 0.25° (Hersbach et al., 2020); 3) the daily precipitation are from the Global Precipitation Climate Program version 1.3 (GPCP v1.3), with a horizontal resolution of 2.5°× 2.5° (Adler et al., 2003); 4) the monthly sea surface wind stress data are provided by the ECMWF Ocean Reanalysis Data (ORAS5), with a horizontal resolution of 1°× 1° (Zuo et al., 2019) and America Ocean Data Assimilation Data Set version 2.2.4 (SODA v2.2.4), with a horizontal resolution of 0.5°× 0.5° (Carton and Giese, 2008); 5) the historical TC data are from the China Meteorological Administration (CMA) tropical cyclone best track dataset (Ying et al., 2014; Lu et al., 2021). All data is detrended before analyzing.

2.3 Diagnostic framework

This study employs a reproducible, model-agnostic diagnostic framework for evaluating resolution-dependent ENSO behavior. Diagnostics include ENSO amplitude and spectrum, Bjerknes feedback decomposition, thermocline and current responses, oceanic zonal current decomposition, and high-frequency (HF) atmospheric variability.

2.3.1 ENSO indices and spectral characteristics

Monthly anomalies of Niño3.4 (5°S–5°N, 170°–120°W) is computed after removing the climatological seasonal cycle. Power spectra are derived using the multi-taper method following Thomson (1982). ENSO irregularity is diagnosed via spectral width and cycle-to-cycle variability.

2.3.2 Bjerknes feedback decomposition

In order to quantitatively analyze the air-sea coupling processes responsible for ENSO amplitude in FGOALS-f3 models, the diagnostic framework of BJ index (Kim and Jin, 2011a, 2011b) is performed in this study. The specific formulation is listed as follows:

$$\mathrm{BJ} = \frac{R-\varepsilon}{2} \quad (1),$$

$$\mathrm{R} = -\left(a_1\frac{\langle\Delta\bar{u}\rangle_E}{L_x} + a_2\frac{\langle\Delta\bar{v}\rangle_E}{L_y}\right) - \alpha_s + \mu_a\beta_u\,\langle-\frac{\partial\bar{T}}{\partial x}\rangle_E + \mu_a\beta_w\,\langle-\frac{\partial\bar{T}}{\partial z}\rangle_E + \mu_a\beta_h a_h\,\langle\frac{\bar{w}}{H_1}\rangle_E \quad (2),$$

$$\frac{\partial\langle h\rangle_w}{\partial \mathrm{t}} = -\varepsilon\langle h\rangle_w - F[\tau_x] \quad (3),$$

$$\langle Q\rangle_E = -\alpha_s\langle T\rangle_E \quad (4),$$

$$\langle H(\bar{w})T_{sub}\rangle_E = a_h\langle T\rangle_E \quad (5),$$

$$\langle h\rangle_E - \langle h\rangle_w = \beta_h[\tau_x] \quad (6),$$

$$\langle H(\bar{w})w\rangle_E = \beta_w[\tau_x] \quad (7),$$

$$\langle u\rangle_E = \beta_u[\tau_x] + \beta_{uh}\langle h\rangle_w \quad (8),$$

$$[\tau_x] = \mu_a\langle T\rangle_E \quad (9),$$

where variables with overbar represent the climatological fields and others denote the anomalous fields obtained by removing the seasonal cycle; *u*, *v*, and *w* are the three dimensional oceanic current velocity; *T* denotes sea surface temperature; $< >_E$ and $< >_W$ represent averaged volume of the eastern box region and western box region, respectively, from the ocean surface to the mixed layer depth; L_x and L_y denote the longitudinal and latitudinal lengths of the eastern box, respectively; H_1 indicates the constant mixed layer depth (65m). The coefficients a_1 and a_2 are obtained through linear regression using SST anomalies (SSTA) zonally or meridionally averaged at the boundaries and area-averaged SSTA over the box. the "Δ" in equation (2) represents the differences of ocean current between the eastern and western boundaries. In equation (3), the first term on the right-hand side are the damping process at the rate of ε; the second term represents the Sverdrup transport across the equatorial Pacific basin. In Equations (4) to (9), α_s indicates the response of the thermodynamic damping to SSTA; μ_a represents the response of surface wind stress anomalies ($\tau_x{}'$) to SSTA; β_u represents the response of upper ocean current anomalies ($u_o{}'$) to $\tau_x{}'$; β_h indicates the response of the anomalous zonal slope of the equatorial Pacific thermocline to $\tau_x{}'$; β_w denotes the response of ocean upwelling anomalies ($w_o{}'$) to $\tau_x{}'$; a_h shows the effect of thermocline depth change on subsurface temperature anomalies. In this study, the computational region is (5°S–5°N, 130°E–90°W).

Based on the above equations, the main contributing terms of the BJ index include two negative feedback processes: the mean advection (MA; $-\left(a_1\frac{\langle\Delta\bar{u}\rangle_E}{L_x}+a_2\frac{\langle\Delta\bar{v}\rangle_E}{L_y}\right)$), the thermodynamic feedback (TD; $-\alpha_s$), and three positive feedback processes: the zonal advection feedback (ZA; $\mu_a\beta_u\langle-\frac{\partial\bar{T}}{\partial x}\rangle_E$), the thermocline feedback (TH; $\mu_a\beta_h a_h\langle\frac{\bar{w}}{H_1}\rangle_E$), and the Ekman feedback (EK; $\mu_a\beta_w\langle-\frac{\partial\bar{T}}{\partial z}\rangle_E$).

2.3.3 HF westerly (easterly) wind index

An index regarding the HF zonal wind anomalies is used to quantitatively measure the intensity of HF westerly (easterly) wind activity in the f3-L and f3-H models. This index (named WWI index and EWI index) is defined as the integration of the averaged zonal HF westerly (easterly) wind over a fixed region (5°S–5°N, 120°E–180°). The formula is as follows:

$$WWI\ \text{index}=\int_{time1}^{time2}u_{HF}{}'dt\ ,\ \ u_{HF}{}'>1m/s \qquad (10),$$

$$EWI\ \text{index}=\int_{time1}^{time2}u_{HF}{}'dt\ ,\ \ u_{HF}{}'<-1m/s \qquad (11),$$

where $u_{HF}{}'$ represents the daily zonal wind anomaly after applying a 90-day high-pass filter, *time1 and time2* represent the start and end time of the integrated period, respectively. In this study, the development period of ENSO event (January to August) is selected as the integrated period.

2.3.4 Oceanic zonal current decomposition

ENSO-related zonal current anomaly (u'_o) in the equatorial region is composed of anomalous zonal geostrophic currents (u'_g) and anomalous Ekman currents (u'_e) (Su et al., 2010; Su et al., 2014). The specific formulas of u'_g and u'_e are listed below:

$$u'_g = -\frac{g\partial^2 D'}{\beta\partial y^2} \quad (12),$$

$$u'_e = \frac{1}{\rho H}\frac{r_s\tau'_x+\beta y\tau'_y}{r_s^2+(\beta y)^2} \quad (13),$$

where β and r_s are the planetary vorticity gradient and Rayleigh dissipation rate (0.5 day^{-1}), respectively; τ'_y denotes the sea meridional wind stress anomaly; H denotes the mean mixed layer depth, and ρ is the seawater density.

2.3.5 TC detection and metrics

The TC detection algorithm developed by the Geophysical Fluid Dynamics Laboratory (https://www.gfdl.noaa.gov/tstorms/; Zhao et al., 2023) was used to detect TC activities in FGOALS-f3 model. The basic identification criteria and steps are: 1) a local minimum SLP is found within a maximum distance of 3,000 km; 2) the wind speed at 850 hPa for this vortex exceed 17 m/s; 3) the absolute value of the vorticity is greater than 1.5×10^{-4} s^{-1}; 4) The temperature within 1200 km of the vortex center is higher than that in the 1200-2400 km radius at 300-500 hPa, indicating a warm core structure; 5) The lifespan of this TC should be at least three days (72h).

We further employ two metrics, i.e, accumulated cyclone energy (ACE) and TC track density (TCTD), to assess the TC activity in FGOALS-f3 models. The ACE index (Bell et al., 2000) in each grid cell is defined as the sum of the squares of the maximum surface wind speeds for all TCs occurring within a 4°×4° grid cell over all 6-hourly periods (i.*e.*, $ACE = \sum_i V_{max}^2$, where i denotes the ith TC in a grid cell and V_{max} denotes its maximum surface wind speed). The TCTD in each grid is defined as the sum of the number of TCs that have passed through the region within a distance of 4°× 4° from the grid center.

3. Evaluation of ENSO Characteristics in f3-L and f3-H

Figure 1 shows the spatial distribution of the standard deviation (STD) of SSTA over the tropical Pacific. In both the high- and low-resolution versions of FGOALS-f3, the interannual variability of SSTA is concentrated in the central-eastern equatorial Pacific (Fig. 1b-c), which is spatially consistent with the observation (Fig. 1a). However, significant differences exist in the ENSO amplitude. Specifically, the STD of the Niño3.4 index is 0.69°C in the observation, 1.53°C in f3-L, and 0.62°C in f3-H, respectively. This indicates that f3-L severely overestimates the ENSO amplitude, whereas f3-H's simulation is much closer to the observation. Considering that the ENSO amplitude simulated in f3-L is approximately 2.5 times that of f3-H, this study will firstly address the causes of the stronger ENSO amplitude in f3-L compared to its counterpart in f3-H.

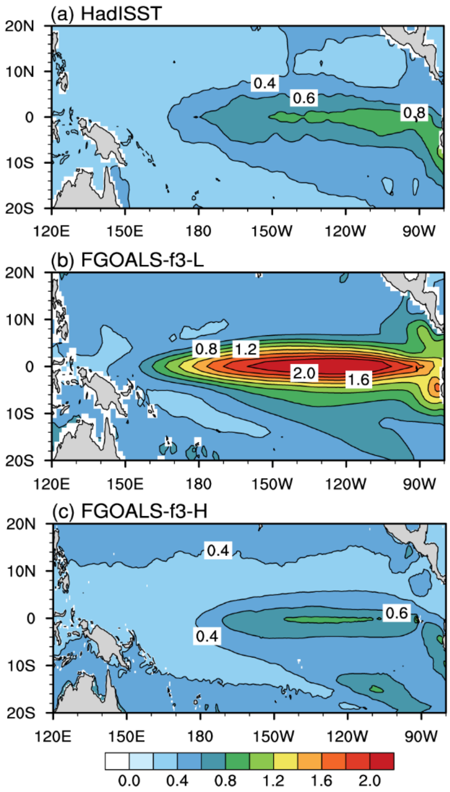

Figure 1. The standard deviation of SSTA (shading, units: °C) for (a) Observation (HadISST), (b) f3-L and (c) f3-H.

Figure 2 presents the time series of the Niño3.4 index for the observation and the two model versions. Obviously, the oscillation intensity of Niño3.4 index in f3-L is much stronger than that in the observation and f3-H, consistent with the results of the STD analysis (Fig. 1). Another notable difference lies in the regularity of the oscillation: ENSO events in f3-L exhibit highly periodic behavior, with a regular transition between warm and cold phases. In contrast, the ENSO evolution in both the observation and f3-H exhibit obvious irregularity. Furthermore, we conduct the power spectrum analysis on the Niño3.4

indices (Fig. 3). In the observation, the power spectrum is characterized by a broad band of 2–8 years. However, the power spectrum in f3-L shows a sharp and significant unimodal peak at approximately 3-year period, with excessive concentration of ENSO energy at this dominant period. In contrast, f3-H reproduces a broadband spectral distribution similar to the observation. Therefore, the second question this study will address is: what causes the overly regular oscillation in f3-L, while f3-H captures more realistic irregularity?

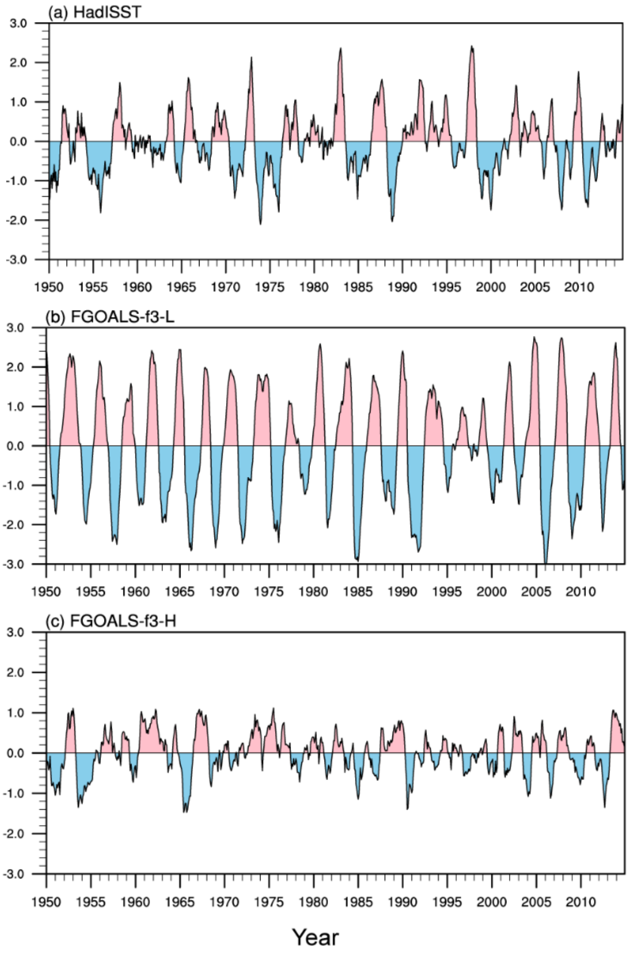

Figure 2. Temporal evolution of Niño3.4 index (the averaged SSTA in the Pacific Niño3.4 region (5°S–5°N, 170°W–120°W), units: °C) for (a) Observation (HadISST), (b) f3-L and (c) f3-H.

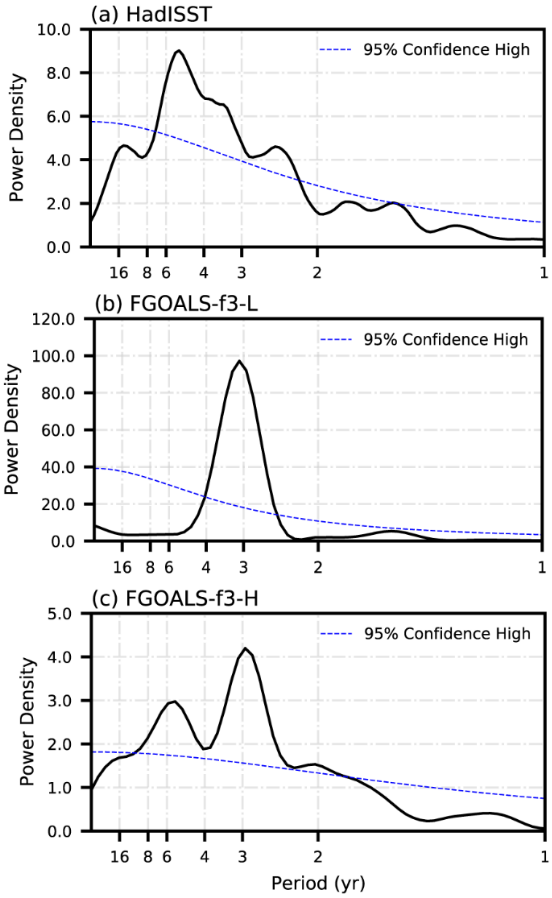

Figure 3. The power spectra of Niño3.4 index for (a) Observation (HadISST), (b) f3-L and (c) f3-H. The blue line in the plots is the 95% confidence level.

4. Process-based Diagnosis of ENSO Amplitude Differences

4.1 Diagnostic analysis based on the BJ index

To investigate the physical mechanisms responsible for the ENSO amplitude difference between the high- and low-resolution versions, we apply the BJ index framework to quantitatively diagnose the stability of the coupled ocean-atmosphere system in both models. Figure 4 presents the BJ index and its five contributing terms for f3-L and f3-H, as well as their difference (f3-L minus f3-H). The results demonstrate that although both models show negative BJ indices, the index value for f3-L is significantly larger (i.e., a smaller negative value) than that for f3-H model. According to the physical interpretation of the BJ index (Jin et al., 2006; Kim and Jin, 2011a; Kim and Jin, 2011b), a smaller absolute value of

BJ index in f3-L indicates that the coupled air-sea system in f3-L is more unstable than that in f3-H. This more unstable coupled system in f3-L is more favorable for ENSO's growth rate, thereby leading to a stronger ENSO amplitude in f3-L than that in f3-H.

A further question arises: which physical processes contribute to the more unstable coupled system in f3-L? By examining the differences in the five contributing terms of the BJ index (orange bars in Fig. 4), we find that the differences in the thermocline feedback (TH) term and the zonal advection feedback (ZA) term are the decisive factors driving the difference in the BJ index (i.e., the system stability) between the high- and low-resolution FGOALS-f3 versions. Therefore, the following analysis will focus on the physical mechanisms responsible for the stronger TH and ZA terms in f3-L relative to f3-H.

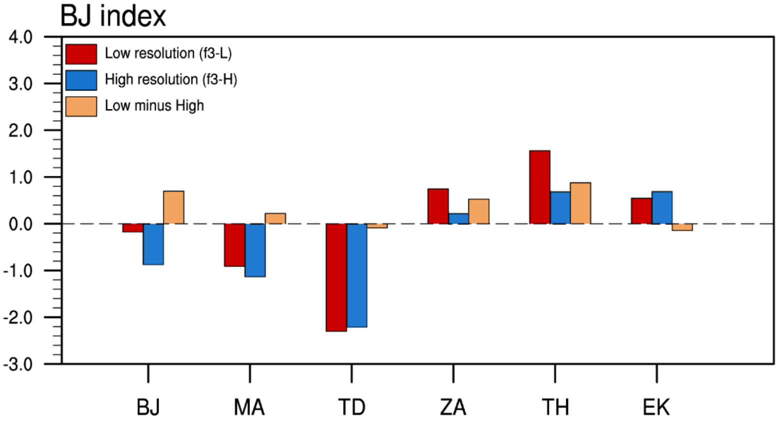

Figure 4. BJ index and the corresponding main contributing terms for the f3-L (red bars), f3-H (blue bars) and their difference (f3-L minus f3-H, orange bars). The five contributing terms including mean advection feedback (MA), thermodynamic damping feedback (TD), zonal advection feedback (ZA), thermocline feedback (TH) and Ekman feedback (EK).

According to the definition of BJ index (see Eq. (2)), each ocean dynamic term consists of two components: one related to the mean state and the other to air-sea feedback processes. Considering that both components may contribute to the differences in ocean dynamic terms between f3-L and f3-H, we first calculate the relative contributions of each component to the total difference in the TH and ZA terms using a total derivative decomposition. As shown in Figure 5a, the stronger TH term in f3-L compared to f3-H (bar 1) primarily comes from the difference in β_h (bar 4). The differences in μ_a and a_h feedback processes make minor contributions, while the mean state differences and the covariance term make negative contributions. Thus, the dominant factor causing the stronger TH term in f3-L is the difference in β_h. Similarly, for the stronger ZA term in f3-L, the results (Fig. 5b) show that the difference in the ZA term (bar 1) is primarily determined by the difference in β_u (bar 4), while the difference in a_h and the covariance change have marginal contribution.

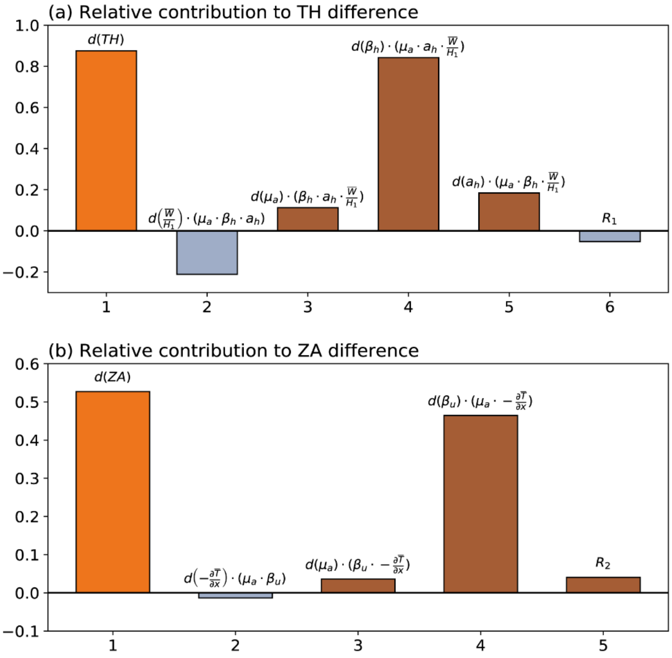

Figure 5. The contribution of each terms in the thermocline feedback (TH). Bar 1 indicate the change of TH term [f3-Lminus f3-H，*d(TH)*]. Bar 2 denotes the contribution from the mean state part change [$d(\overline{w}/H_1)$] to the change of TH term. Bar 3, Bar 4 and Bar 5 indicate the contribution from the air-sea feedbacks [$d(\mu_a)$, $d(\beta_h)$and $d(a_h)$] to the change of TH feedback, respectively. Bar 6 is the residual, which denotes the contribution from the covariant changes of both the mean state part and the air-sea feedbacks. (b) The contribution of each terms in the zonal advection feedback (ZA). Bar 1 indicate the change of ZA term [f3-L minus f3-H，*d(ZA)*]. Bar 2 denotes the contribution from the mean state part change [$d(\partial\overline{T}/\partial x)$] to the change of TH term. Bar 3 and Bar 4 indicate the contribution from the air-sea feedbacks [$d(\mu_a)$ and $d(\beta_u)$] to the change of ZA feedback, respectively. Bar 5 is the residual, which denotes the contribution from the covariant changes of both the mean state part and the air-sea feedbacks.

4.2 Resolution dependence of the β_h feedback process difference

The air-sea feedback process β_h represents the response of the equatorial Pacific thermocline tilt to $\tau_x{}'$. Figure 6 shows the regression of thermocline depth anomalies onto zonal wind stress anomalies for the two models. Both models reproduce the expected pattern: in response to positive $\tau_x{}'$ over the equatorial Pacific, the anomalous thermocline depth (D') deepens in the eastern equatorial Pacific and shoals in the western equatorial Pacific. However, the response is much stronger in f3-L than in f3-H.

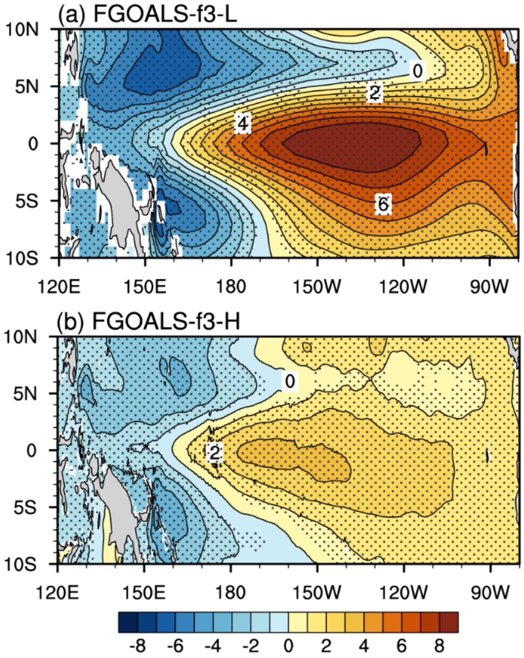

Figure 6. Distribution of the response of thermocline depth anomaly to zonal wind stress anomaly [β_h; units: m (N m^{-2})$^{-1}$] for (a) f3-L and (b) f3-H. Based on the linear relationship between sea surface height anomaly (SSHA) and thermocline depth anomaly (D'), the SSHA is used as a proxy of D'. The D' response to zonal wind stress anomaly is derived through regressing the SSHA field onto the averaged zonal wind stress anomaly over equatorial Pacific (5°S–5°N, 120°E–100°W). The stippling in this plot denotes the regression coefficient exceeding a confidence level of 99% by using Student's *t* test.

Based on the Sverdrup balance relationship (Jin, 1997; Li, 1997), the response of the D' to $\tau_x{}'$ is primarily determined by the mean equatorial thermocline depth ($\overline{H}$) and $\tau_x{}'$:

$$\frac{\partial D'}{\partial x} = \frac{\tau_x'}{\rho g \overline{H}} \qquad (14),$$

where ρ is the seawater density and g is the reduced gravity. We first examine the mean thermocline depth in both models and find that the difference in $\overline{H}$ between f3-L and f3-H is negligible (figure not shown). Therefore, the difference in $\overline{H}$ is not the primary cause.

Previous studies (Chen et al., 2015b; Chen et al., 2019) have pointed out that the meridional structure of $\tau_x{}'$ is another key factor influencing the strength of β_h. Figure 7a presents the meridional structure of $\tau_x{}'$ for the two models and their difference (orange, f3-L minus f3-H). A significant difference exists: although the regression results show the same magnitude of $\tau_x{}'$ within the equatorial Pacific (5°S–5°N), the $\tau_x{}'$ in f3-L is meridionally more concentrated near the equator (0°) than that in f3-H. Since the $\tau_x{}'$ closer to equator is more effective in influencing D' (Chen et al., 2015b; Chen et al., 2019), this more equatorially-confined meridional structure of $\tau_x{}'$ in f3-L inevitably results in a stronger response of D' to $\tau_x{}'$ (i.e., a larger β_h).

Furthermore, we compare the meridional structure of ENSO-related τ'_x in the two model versions with two reanalysis datasets. As shown in Fig. 7b, the meridional structures of τ'_x in the two reanalysis products (black lines) are very similar between 10°S–5°N, while some discrepancies exist within 5°N–10°N region. For the models, the f3-H (25 km atmospheric resolution) shows a τ'_x meridional structure in the equatorial region (5°S–5°N) that substantially resembles both reanalysis datasets. In contrast, the meridional structure of τ'_x within 5°S–5°N in f3-L (100 km atmospheric resolution) shows obvious discrepancies from the two reanalysis datasets. This suggests that model horizontal resolution can influence ENSO simulation by affecting the meridional distribution of τ'_x. The higher horizontal resolution is conducive to the more realistic representation of equatorial τ'_x meridional structure, thereby yielding a more reasonable thermocline feedback and ENSO amplitude.

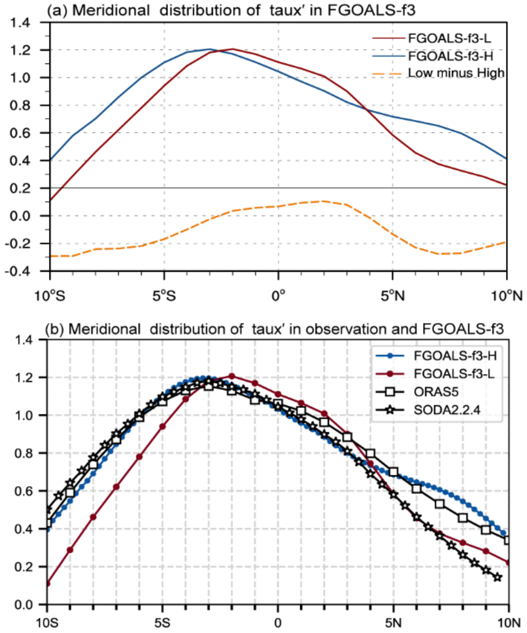

Figure 7. Meridional structure of normalized zonal wind stress anomalies [units: N m^{-2} (N m^{-2})$^{-1}$] averaged over the Niño4 longitude range (160°E–150°W) for (a) the result of f3-L (red solid line), f3-H (blue solid line) and their difference (orange dash line, f3-L minus f3-H). In this plot, all the data are both interpolated onto a 1° x 1° grid to facilitate the comparison; (b) the results of ORAS5 (black line marked by square, with a 1° x 1° grid), SODA2,2,4 (black line marked by asterisk, with a 0.25° x 0.25° grid), f3-L (red line marked by circle, with a 1° x 1° grid) and f3-H (blue line marked by circle, with a 0.25° x 0.25° grid). The normalized zonal wind stress anomalies are obtained

by regressing the zonal wind stress anomalies field onto the Niño4 region (5°S–5°N, 160°E–150°W) averaged zonal wind stress anomalies.

4.3 Resolution dependence of of the β_u feedback process

The air-sea feedback process β_u represents the response of the equatorial Pacific upper ocean zonal current anomaly (u_o') to τ_x'. Figure 8 shows the equatorial profile for the response of u_o' to τ_x' in both models. Both models simulate eastward u_o' a unit eastward τ_x' in equatorial Pacific, but the response is significantly stronger in f3-L than in f3-H.

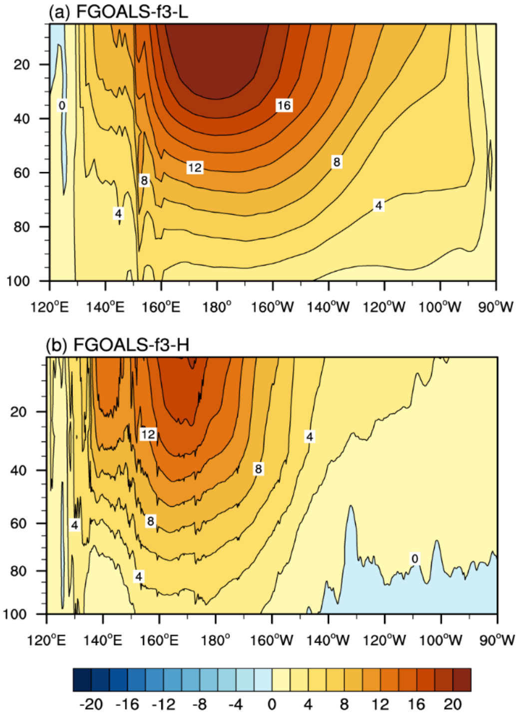

Figure 8. Vertical profile (averaged over 5°S–5°N) of the response of zonal ocean current anomaly (u_o') to the zonal wind stress anomaly [β_u; units: m s^{-1} (N m^{-2})$^{-1}$] for (a) f3-L and (b) f3-H. The u_o' response to zonal wind stress anomaly is derived through regressing the u_o' field onto the averaged zonal wind stress anomaly over equatorial Pacific (5°S–5°N, 120°E–100°W).

Considering that ENSO-related u_o' in the equatorial region is composed of anomalous zonal geostrophic currents (u_g') and anomalous Ekman currents (u_e') (see Section 2.3.4), we first diagnose the response of u_g' and u_e' to wind stress anomalies (Fig. 9). In both versions, the response of u_o' to τ_x' is primarily contributed by the response of u_g' to τ_x', while the contribution of u_e' is much smaller. This indicates that the difference in u_g' response to τ_x' is the main cause of the difference in β_u

between the two model versions. Based on the geostrophic formula (Eq. (12)), the magnitude of u_g' is related to the second-order meridional derivative of D'. Since the meridional structure of D' (Figure 6) exhibits a parabolic shape (peaking at equator and decreasing poleward), a stronger D' in the equatorial region corresponds to a larger value of second-order meridional derivative ($-\frac{\partial^2 D'}{\partial y^2}$) and, consequently, a stronger u_g'. As the D' response to τ_x' is primarily modulated by the $\beta_{\hbar}$ process, the difference in the β_u between the f3-L and f3-H is also primarily attributed to difference in the $\beta_{\hbar}$ process. That is, the stronger $\beta_{\hbar}$ in f3-L leads to a stronger D', which in turn induces a stronger u_g' and u_o' and ultimately resulting in a stronger β_u.

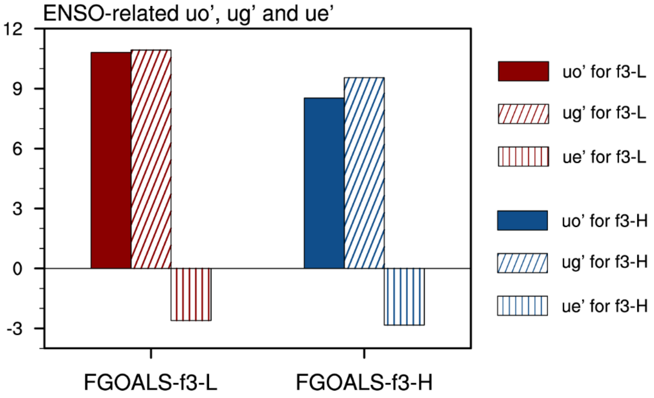

Figure 9. The ENSO-related zonal current anomalies (u') averaged over 0–65m, zonal geostrophic current anomalies (u_g') and zonal Ekman current anomalies (u_e') along the equatorial eastern Pacific (2ºS–2ºN, 180º–80ºW) for f3-L (red bar) and f3-H (blue bar). The ENSO-related zonal current anomalies, zonal geostrophic current anomalies and zonal Ekman current anomalies are obtained by regressing it anomalies field onto the zonal wind stress anomalies averaged over Niño4 region (5°S–5°N, 160°E–150°W), respectively.

4.4 Comparison with OMIP simulations

It should be noted that although our conclusions drawn from Coupled General Circulation Model (CGCM) indicate that the improved ENSO simulation is closely linked to the increased atmospheric resolution, the potential influence of oceanic horizontal resolution on ENSO simulation also merits brief examination. For instance, from the perspective of the oceanic component of CGCM (OGCM), Li et al. (2025) examined the oceanic zonal current and thermocline depth anomalies to zonal wind forcing by analyzing the outputs from Ocean Model Intercomparison Project 2 (OMIP2, Griffies et al. 2016) and found that the oceanic response to wind forcing is a key influencing ENSO simulation. According to the

https://doi.org/10.5194/egusphere-2025-6017
Preprint. Discussion started: 21 January 2026

CMIP6's protocol, OMIP2 experiments are forced by the identical atmospheric reanalysis datasets, thus providing an ideal framework to isolate biases originating from the oceanic component. Both f3-L and f3-H have participated in OMIP2, with respective oceanic horizontal resolutions of approximately 1° and 0.1°. To further assess the potential impact of oceanic horizontal resolution on ENSO simulation, we compare the key air-sea feedback terms ($\beta_{\hbar}$ and β_u) between f3-L and f3-H OMIP2 outputs. As shown in figure 10, the response of zonal current and thermocline depth anomalies to the identical τ_x' are remarkably similar between the two ocean models. This indicates that the differences in OGCM resolution itself may be not the primary driver of the differences in $\beta_{\hbar}$ and β_u. Moreover, this finding (Fig. 10) stands in stark contrast to the large differences in $\beta_{\hbar}$ and β_u identified in the two coupled simulations (Figures 6 and 8). Therefore, the evidence from the OMIP2 experiments corroborates our main conclusion: the refined atmospheric horizontal resolution, which more realistically captures the meridional structure of τ_x', plays a decisive role in improving the simulation of the key air-sea feedbacks ($\beta_{\hbar}$ and β_u) and ENSO amplitude in FGOALS-f3 model. Nevertheless, a more comprehensive investigation, potentially involving finer oceanic resolutions and their interactions with the atmosphere, deserves further exploration in the future.

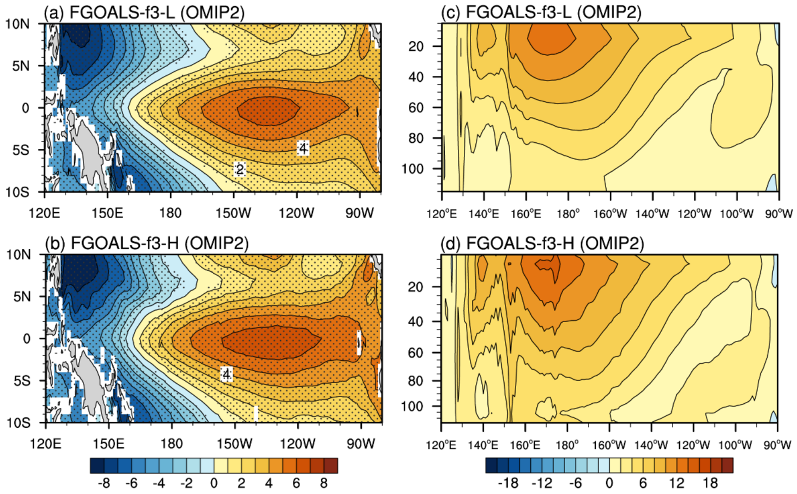

Figure 10. (a)–(b) and (c)–(d) are same as Figure 6 and 8, respectively, but for the OMIP2 simulations.

5. Diagnostic of Oscillation Regularity

5.1 Resolution dependence of ENSO irregularity: Differences in HF wind activity

A large body of studies have suggested that the HF zonal wind activity over the western and central equatorial Pacific (WCEP) plays a crucial role in the onset and development of ENSO events (Rong et al., 2011; Chen et al., 2017). In general, this HF zonal wind activity refers to westerly wind event (WWE) and easterly wind event (EWE) with time scales less than 90 days. Due to their transient, intense, and somewhat random nature, the HF zonal wind forcing is also considered as an important factor contributing to the diversity and irregularity of ENSO (Chen et al., 2015a; Fedorov et al., 2015). Motivated by this, we hypothesize that the difference in the ENSO regularity between f3-L and f3-H may arise from the differences in HF zonal wind activity.

To test this, we calculate the intensity of the HF zonal wind activity based on the Equations (10) and (11). Figure 11 shows the WWI and EWI index that measures the cumulative sum of HF westerly (easterly) wind anomalies over WCEP during the ENSO development period, for the observation and the two model versions. As shown in Figure 11a, the intensity of HF westerlies in f3-H is comparable to that in the observation, with similar mean and median values. However, f3-L simulates much weaker intensity of HF westerlies. For HF easterly activity (Fig. 11b), both models show comparable statistics to the observation, with no significant differences between f3-L and f3-H. Overall, these results indicate that f3-L strongly underestimates HF westerly wind activity relative to the f3-H and the observation.

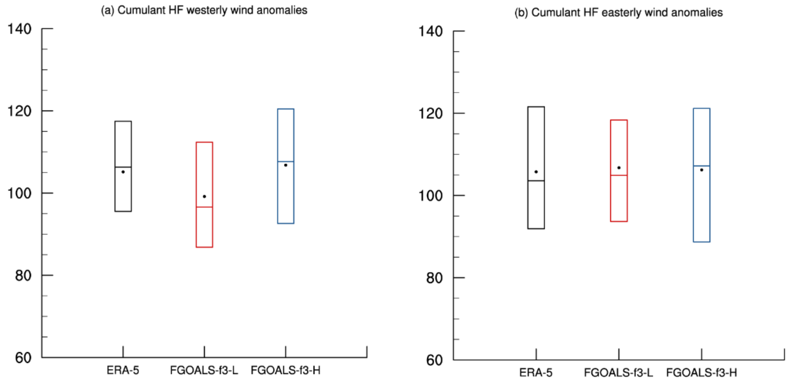

Figure 11. The boxplots of the (a) WWI index and (b) EWI index during the ENSO development phase (January to August). Red, blue and black boxes indicate the f3-L, f3-H and observations, respectively. The upper and lower boundaries of the box represent the 75th and 25th percentile values, respectively. The horizontal line in the box represents the median. The black dot represents the average value.

https://doi.org/10.5194/egusphere-2025-6017
Preprint. Discussion started: 21 January 2026

HF westerly wind activities are considered as semi-stochastic perturbations that modulate ENSO evolution (Gebbie et al., 2007; Gebbie and Tziperman, 2009). On the one hand, their occurrence is partly influenced by ENSO-related SSTA (Sun et al., 2020), but is also regarded as random noise independent of ENSO system (Moore and Kleeman, 1999). Most ENSO theoretical models treat HF westerly wind activity as external white noise forcing (Eisenman et al., 2005). This implies that the impact of HF activity on the coupled system depends, to some extent, on its relative magnitude relative to the ENSO amplitude. Notably, the aforementioned analysis based on the BJ index (a linear framework that excludes nonlinear processes like atmospheric "noise") has shown that the coupled system simulated by f3-L is more unstable than that of f3-H, hence the ENSO variability in f3-L is more prone to self-sustained oscillation. Considering that the HF wind activities in f3-L is also significantly weaker than that in f3-H, from the perspective of signal-to-noise ratio, this weaker "noise" is insufficient to "disrupt" the overly strong ENSO oscillation in f3-L, allowing its ENSO cycle to evolve in a regular and self-sustained manner.

5.2 Sources of differences in HF westerly wind activity: evaluation of TC and MJO

To further explore the origin of difference in HF westerly wind intensity between f3-L and f3-H, we compare the simulated performance of TC and MJO activities in these two models. The results show that the differences in the HF westerly wind intensity are primarily related to the models' ability to reproduce TC activity. Figure 12 shows the spatial distribution of TCTD over the western North Pacific (WNP). The spatial distributions of TCTD in both f3-H and f3-L are similar to the observation, with TC tracks primarily located in the southwestern quadrant of WNP. Although both versions can reasonably reproduce the spatial distribution characteristics of TC activities over the WNP, a significant difference exists in TC frequency: TC activity is much more frequent in f3-H than that in f3-L. The difference map (Fig. 12d, f3-H minus f3-L) shows positive values almost everywhere north of the equator. It is worth noting that TCTD in f3-H remains relatively weak compared to the observation, which is a common simulation bias in most current climate models (Nakamura et al., 2017; Tang et al., 2022). Although f3-H still underestimates TC activity compared to the observation, this improvement relative to f3-L is substantial.

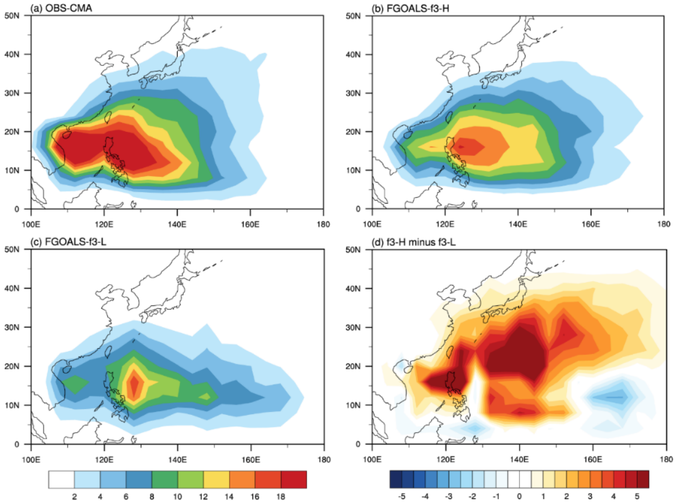

Figure 12. The averaged TC track density (TCTD, units: counts year^{-1}) over western North Pacific for (a) Observation (CMA), (b) f3-H, (c) f3-L and (d) the difference between f3-H and f3-L (f3-H minus f3-L).

Furthermore, we compare the difference in the TC intensity between f3-H and f3-L. Figure 13 shows the spatial distribution of ACE index over WNP in the observation and the models. Both models show that strong TC activity is primarily concentrated east of the Philippines sea, consistent with the observation (Ma et al., 2025). However, the ACE index in f3-H is significantly stronger than that in f3-L, indicating stronger TC activity in f3-H. In summary, the TC activity over WNP is more frequent and intense in f3-H than that in f3-L, which largely explains the stronger HF westerly wind anomalies in f3-H.

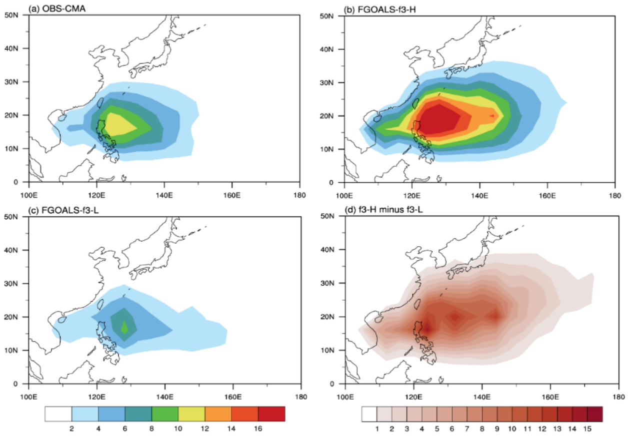

Figure 13. The averaged accumulated cyclone energy (ACE, units: 10^4 knots year^{-1}) over western North Pacific for (a) Observation (CMA), (b) f3-H, (c) f3-L and (d) the difference between f3-H and f3-L (f3-H minus f3-L).

https://doi.org/10.5194/egusphere-2025-6017
Preprint. Discussion started: 21 January 2026

Model horizontal resolution is a key factor in TC simulation (Tang et al., 2022). In general, climate models with coarse resolutions (≥ 100 km) tend to only reproduce TC-like structures (Camargo et al., 2005; Camargo and Wing, 2016), with activity that is relatively weak and infrequent (Camargo, 2013; Nakamura et al., 2017). As resolution increases, models can simulate more frequent and more intense TC activity (Roberts et al., 2020a; Tang et al., 2022). In particular, when the horizontal resolution is increased to 25 km, the simulation of TC spatial structure and associated wind fields is significantly improved, yielding a more realistic characteristics of TC activity (Davis et al., 2018; Roberts et al., 2020b). The analysis results of the FGOALS-f3 models (Figs. 11 and 12) are consistent with these previous findings. Compared to the f3-L model (with a horizontal resolution of 100 km), the f3-H model (with a horizontal resolution of 25 km) provides a more realistic simulation of TC frequency and produces stronger TC intensities. This difference in TC simulation associated with model resolution modulates the intensity of HF westerly wind activity and hence influences the regularity of ENSO cycle in the two models.

On the other hand, we also examine the other primary source of HF westerly wind activity–the MJO. Figure 14 shows the wavenumber-frequency spectra of the space-time filtered precipitation and surface zonal wind. It can be seen that the spectral peak of precipitation and surface zonal wind in both models are concentrated at 30-80-day period, consistent with the observation. This indicates that both models reproduce the observed MJO timescales reasonably well. In terms of intensity, although the MJO-related precipitation and zonal wind fields are somewhat exaggerated in both models compared to the observation, the difference between f3-L and f3-H is small, especially for MJO-related zonal winds. Therefore, the difference in HF westerly wind activity is likely not directly linked to MJO activity.

Although finer resolution may improve model performance in certain aspects, these preliminary results show no significant improvement in MJO simulation from 100 km to 25 km in the case of these two FGOALS-f3 models. On the one hand, this may be because MJO simulation is heavily constrained by the accurate representation of physical processes like convection parameterization, boundary layer processes, and air-sea coupling. Thus, increased resolution must be combined with optimized physics schemes to effectively improve MJO simulation (Jiang et al., 2020b). On the other hand, recent studies suggest that significant MJO improvement can be seen when resolution increases to the kilometer-scale–the "convection-permitting resolution" (Savarin and Chen, 2022).

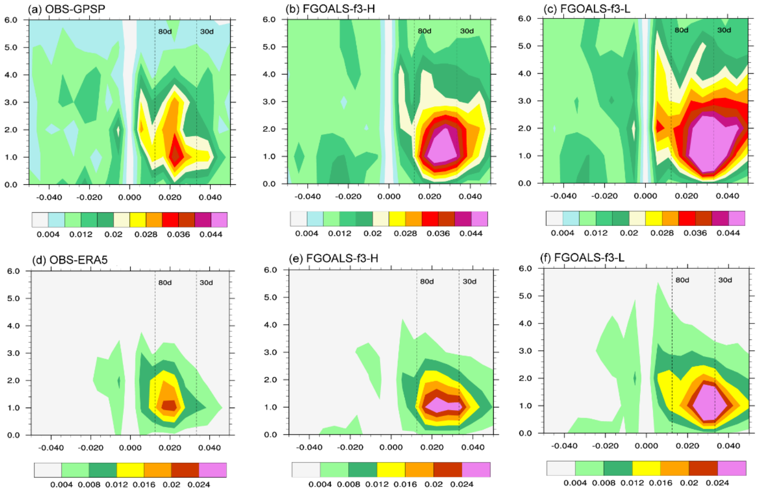

Figure 14. Wavenumber-frequency spectra of space-time filtered (a)–(c) precipitation (units: mm/day) and (d)–(f) surface zonal wind fields (m/s) during the boreal winter (November to next August) for observation (left column), f3-H (middle column) and f3-L (right column).

In summary, we find that the high-resolution version can better simulate TC activity, with more frequent and stronger TCs over the WNP than the lower-resolution version. This difference results in stronger HF westerly wind activity in f3-H than that in f3-L. Given that HF westerly wind activity acts as a stochastic forcing on ENSO, the relatively weaker HF atmospheric noise in f3-L has a limited randomizing effect on its stronger ENSO signal. In other words, the weaker HF zonal wind activity in f3-L cannot overcome its inherently stronger ENSO signal, leading to overly regular oscillation in f3-L. In contrast, f3-H has a weaker intrinsic ENSO signal but stronger "noise". Therefore, the ENSO cycle in f3-L appears much more regular than that in f3-H.

6. Conclusions and implications

6.1 Conclusions

This study provides a process-based evaluation of how horizontal resolution influences ENSO simulation in the CAS FGOALS-f3 climate system model. The comparison between its low-resolution (f3-L) and high-resolution (f3-H) configurations reveals systematic and resolution-dependent differences in ENSO amplitude, period, oscillation characteristics and underlying air-sea coupling processes.

A key structural source of bias in f3-L is the overly confined meridional structure of ENSO-related zonal wind stress anomalies, which strengthens the thermocline and zonal-advection feedbacks and leads to an exaggerated ENSO amplitude. The process-oriented diagnosis based on ENSO-related air-sea coupling processes demonstrates that these feedbacks can be directly attributed to resolution-sensitive wind stress structures, indicating that resolving the meridional structure of wind forcing is essential for realistic representation of ENSO amplitude.

The excessive regularity of ENSO in f3-L is another resolution-driven bias, arising from insufficient HF atmospheric variability. The high-resolution configuration produces more realistic TC activity and vigorous WWEs, which introduce stochastic forcing that disrupts the ENSO cycle and generates irregular variability. These results highlight that the representation of synoptic-scale atmospheric processes is integral to capturing realistic ENSO temporal evolution.

Overall, this study demonstrates that ENSO-related biases in FGOALS-f3 arise from identifiable, resolution-sensitive structural features in the coupled system. By quantifying feedback pathways and stochastic forcing, we provide a traceable explanation for how horizontal resolution modulates ENSO simulation. The evaluation framework developed here offers a practical tool for diagnosing ENSO performance in other climate models and can guide future development of the FGOALS-f3 model family.

6.2 Implications

The findings from this study yield several actionable insights for FGOALS-f3 development and for the broader CMIP-class modeling community. (1) Improving the atmospheric representation of equatorial wind stress gradients should be a development priority. (2) Resolution has complementary impacts on deterministic and stochastic ENSO dynamics: the deterministic aspect influencing ENSO simulation is via air–sea coupling processes, and the stochastic aspect influencing ENSO simulation is via high-frequency wind activity (e.g., WWE), whose dual role should be explicitly considered in future model evaluation framework. (3) The diagnostics applied here are model-agnostic and can serve as a reproducible framework for assessing resolution effects in other climate models participating in CMIP6/CMIP7. (4) The ~25 km atmosphere resolution of f3-H improves both the air-sea coupling processes and the stochastic forcing mechanisms. This supports the ongoing efforts toward next-generation high-resolution models.

Data and Code availability. Source codes of the FGOALS-f3 model used in this study and the analysis scripts are archived at https://doi.org/https://doi.org/10.5281/zenodo.17778266 (Song, 2025). The model output of FGOALS-f3 models described in this paper is distributed through the Earth System Grid Federation (ESGF) and is freely obtained via the ESFG data portals after registration (https://aims2.llnl.gov/search, last access: 27 November 2025). All the observation and reanalysis datasets are available online and publicly available as cited in the references. The ORAS5 and ERA-5 datasets are obtained from https://cds.climate.copernicus.eu/datasets. The HadISST dataset is from https://www.metoffice.gov.uk/hadobs/hadisst/data/download.html. The GPCP dataset is available at https://www.ncei.noaa.gov/data/global-precipitation-climatology-project-gpcp-daily/access. The SODA2.2.4 dataset can be accessed at http://apdrc.soest.hawaii.edu/datadoc/soda_2.2.4.php. The CMA TC best track dataset is from https://tcdata.typhoon.org.cn/en/zjljsjj.html. The description and data for HighResSST-present simulations of FGOALS-f3 can be found at http://doi.org/10.22033/ESGF/CMIP6.3312 (Bao and He, 2019; Bao et al., 2020).

Author contribution. All authors contributed to the study conception and design. Material preparation, data collection and analysis were performed by MS and LC. JZ contributed to the application of methods related to TC detection. The first draft of the manuscript was written by MS, LC and QY contributed to the writing and revising of the manuscript. BA and HZ discussed the results and commented on the manuscript. All authors read and approved the final manuscript.

Competing interests. The authors declare that they have no conflict of interest.

Acknowledgements. We acknowledge the High Performance Computing Center of Nanjing University of Information Science & Technology for their support of this work.

Financial support. This work was the jointly supported by the National Key Research and Development Program of China (Grant 2022YFF0802004), NSFC (No. 42576024), the Excellent Youth Natural

Science Foundation of Jiangsu Province (BK20230061) and Postgraduate Research & Practice Innovation Program of Jiangsu Province (KYCX24_1417).

Reference

Adler, R. F., Huffman, G. J., Chang, A., Ferrao, R., Xie, P.-P., Janowiak, J., Rudolf, B., Schneiser, U., Curtis, S., Bolvin, D., Gruber, A., Susskind, J., Arkin, P., and Nelkin, E.: The version-2 global precipitation climatology project (GPCP) monthly precipitation analysis (1979–present), Journal of Hydrometeorology, 4, 1147–1167, https://doi.org/10.1175/1525-7541(2003)004%3C1147:TVGPCP%3E2.0.CO;2, 2003.

An, B., Yu, Y. Q., Bao, Q., He, B., Li, J. X., Luan, Y. H., Chen, K. J., and Zheng, W. P.: CAS FGOALS-f3-H dataset for the high-resolution model intercomparison project (HighResMIP) Tier 2, Advances in Atmospheric Sciences, 39, 1873–1884, https://doi.org/10.1007/s00376-022-2030-5, 2022.

Bacmeister, J. T., Wehner, M. F., Neale, R. B., Gettelman, A., Hannay, C., Lauritzen, P. H., Caron, J. M., and Truesdale, J. E.: Exploratory high-resolution climate simulations using the community atmosphere model (CAM), Journal of Climate, 27, 3073–3099, https://doi.org/10.1175/jcli-d-13-00387.1, 2014.

Bao, Q., Liu, Y. M., Wu, G. X., He, B., Li, J. X., Wang, L., Wu, X. F., Chen, K. J., Wang, X. C., Yang, J., and Zhang, X. Q.: CAS FGOALS-f3-H and CAS FGOALS-f3-L outputs for the high-resolution model intercomparison project simulation of CMIP6, Atmospheric and Oceanic Science Letters, 13, 576–581, https://doi.org/10.1080/16742834.2020.1814675, 2020.

Bao, Q. and He, B.: CAS FGOALS-f3-H model output prepared for CMIP6 HighResMIP highresSST-present, Earth System Grid Federation [data set], https://doi.org/10.22033/ESGF/CMIP6.3312, 2019

Barnston, A. G., Tippett, M. K., L'Heureux, M. L., Li, S., and DeWitt, D. G.: Skill of real-time seasonal ENSO model predictions during 2002–11: Is our capability increasing?, Bulletin of the American Meteorological Society, 93, 631–651, https://doi.org/10.1175/bams-d-11-00111.1, 2012.

Bell, G. D., Halpert, M. S., Schnell, R. C., Higgins, R. W., Lawrimore, J., Kousky, V. E., Tinker, R.,

https://doi.org/10.5194/egusphere-2025-6017
Preprint. Discussion started: 21 January 2026

Thiaw, W., Chelliah, M., and Artusa, A.: Climate assessment for 1999, Bulletin of the American Meteorological Society, 81, s1–s50, https://doi.org/10.1175/1520-0477(2000)81[s1:CAF]2.0.CO;2, 2000.

Cai, W. J., Santoso, A., Collins, M., Dewitte, B., Karamperidou, C., Kug, J.-S., Lengaigne, M., McPhaden, M. J., Stuecker, M. F., Taschetto, A. S., Timmermann, A., Wu, L. X., Yeh, S.-W., Wang, G., Ng, B., Jia, F., Yang, Y., Ying, J., Zheng, X.-T., Bayr, T., Brown, J. R., Capotondi, A., Cobb, K. M., Gan, B., Geng, T., Ham, Y.-G., Jin, F.-F., Jo, H.-S., Li, X., Lin, X., McGregor, S., Park, J.-H., Stein, K., Yang, K., Zhang, L., and Zhong, W. X.: Changing El Niño–Southern Oscillation in a warming climate, Nature Reviews Earth and Environment, 2, 628–644, https://doi.org/10.1038/s43017-021-00199-z, 2021.

Camargo, S. J., Barnston, A. G., and Zebiak, S. E.: A statistical assessment of tropical cyclone activity in atmospheric general circulation models, Tellus A: Dynamic Meteorolgy and Oceanography, 57, 589–604, https://doi.org/10.3402/tellusa.v57i4.14705, 2005.

Camargo, S. J.: Global and regional aspects of tropical cyclone activity in the CMIP5 models, Journal of Climate, 26, 9880–9902, https://doi.org/10.1175/jcli-d-12-00549.1, 2013.

Camargo, S. J. and Wing, A. A.: Tropical cyclones in climate models, Wiley Interdisciplinary Reviews: Climate Change, 7, 211–237, https://doi.org/10.1002/wcc.373, 2016.

Carton, J. A. and Giese, B. S.: A Reanalysis of Ocean Climate Using Simple Ocean Data Assimilation (SODA), Monthly Weather Review, 136, 2999–3017, https://doi.org/10.1175/2007mwr1978.1, 2008.

Chang, P., Zhang, S. Q., Danabasoglu, G., Yeager, S. G., Fu, H. H., Wang, H., Castruccio, F. S., Chen, Y., Edwards, J., Fu, D., Jia, Y., Laurindo, L. C., Liu, X., Rosenbloom, N., Small, R. J., Xu, G. P., Zeng, Y. H., Zhang, Q. Y., Bacmeister, J., Bailey, D. A., Duan, X., DuVivier, A. K., Li, D. P., Li, Y. X., Neale, R., Stössel, A., Wang, L., Zhuang, Y., Baker, A., Bates, S., Dennis, J., Diao, X., Gan, B. L., Gopal, A., Jia, D. N., Jing, Z., Ma, X., Saravanan, R., Strand, W. G., Tao, J., Yang, H. Y., Wang, X. Q., Wei, Z. Q., and Wu, L. X.: An unprecedented set of high-resolution earth system simulations for understanding multiscale interactions in climate variability and change, Journal of Advances in Modeling Earth Systems, 12, e2020MS002298, https://doi.org/10.1029/2020ms002298, 2020.

Chen, D. K., Lian, T., Fu, C., Cane, M. A., Tang, Y. M., Murtugudde, R., Song, X. S., Wu, Q. Y., and

Zhou, L.: Strong influence of westerly wind bursts on El Niño diversity, Nature Geoscience, 8, 339–345, https://doi.org/10.1038/ngeo2399, 2015a.

Chen, L., Li, T., and Yu, Y. Q.: Causes of strengthening and weakening of ENSO amplitude under global warming in four CMIP5 models, Journal of Climate, 28, 3250–3274, https://doi.org/10.1175/jcli-d-14-00439.1, 2015b.

Chen, L., Yu, Y. Q., and Zheng, W. P.: Improved ENSO simulation from climate system model FGOALS-g1.0 to FGOALS-g2, Climate Dynamics, 47, 2617–2634, https://doi.org/10.1007/s00382-016-2988-8, 2016.

Chen, L., Li, T., Wang, B., and Wang, L.: Formation mechanism for 2015/16 super El Nino, Scientific Reports, 7, 2975–2985, https://doi.org/10.1038/s41598-017-02926-3, 2017.

Chen, L., Wang, L., Li, T., and Liu, J.: Drivers of reduced ENSO variability in mid-Holocene in a coupled model, Climate Dynamics, 52, 5999–6014, https://doi.org/10.1007/s00382-018-4496-5, 2019.

Craig, A. P., Vertenstein, M., and Jacob, R.: A new flexible coupler for earth system modeling developed for CCSM4 and CESM1, The International Journal of High Performance Computing Applications, 26, 31–42, https://doi.org/10.1177/1094342011428141, 2012.

Davis, C. A.: Resolving tropical cyclone intensity in models, Geophysical Research Letters, 45, 2082–2087, https://doi.org/10.1002/2017GL076966, 2018.

Dawson, A., Matthews, A. J., Stevens, D. P., Roberts, M. J., and Vidale, P. L.: Importance of oceanic resolution and mean state on the extra-tropical response to El Niño in a matrix of coupled models, Climate Dynamics, 41, 1439–1452, https://doi.org/10.1007/s00382-012-1518-6, 2013.

Docquier, D., Grist, J. P., Roberts, M. J., Roberts, C. D., Semmler, T., Ponsoni, L., Massonnet, F., Sidorenko, D., Sein, D. V., Iovino, D., Bellucci, A., and Fichefet, T.: Impact of model resolution on Arctic sea ice and North Atlantic Ocean heat transport, Climate Dynamics, 53, 4989–5017, https://doi.org/10.1007/s00382-019-04840-y, 2019.

Eisenman, I., Yu, L. S., and Tziperman, E.: Westerly wind bursts: ENSO's tail rather than the dog?, Journal of Climate, 18, 5224–5237, https://doi.org/10.1175/JCLI3588.1, 2005.

Eyring, V., Bony, S., Meehl, G. A., Senior, C. A., Stevens, B., Stouffer, R. J., and Taylor, K. E.: Overview of the Coupled Model Intercomparison Project Phase 6 (CMIP6) experimental design and organization, Geoscientific Model Development, 9, 1937–1958, https://doi.org/10.5194/gmd-9-

1937-2016, 2016.

Fedorov, A. V.: The response of the coupled tropical ocean–atmosphere to westerly wind bursts, Quarterly Journal of the Royal Meteorological Society, 128, 1–23, https://doi.org/10.1002/qj.200212857901, 2002.

Fedorov, A. V., Hu, S. N., Lengaigne, M., and Guilyardi, E.: The impact of westerly wind bursts and ocean initial state on the development, and diversity of El Niño events, Climate Dynamics, 44, 1381–1401, https://doi.org/10.1007/s00382-014-2126-4, 2015.

Gebbie, G., Eisenman, I., Wittenberg, A., and Tziperman, E.: Modulation of westerly wind bursts by sea surface temperature: A semistochastic feedback for ENSO, Journal of the Atmospheric Sciences, 64, 3281–3295, https://doi.org/10.1175/jas4029.1, 2007.

Gebbie, G. and Tziperman, E.: Incorporating a semi-stochastic model of ocean-modulated westerly wind bursts into an ENSO prediction model, Theoretical and Applied Climatology, 97, 65–73, https://doi.org/10.1007/s00704-008-0069-6, 2009.

Griffies, S. M., Danabasoglu, G., Durack, P. J., Adcroft, A. J., Balaji, V., Böning, C. W., Chassignet, E. P., Curchitser, E., Deshayes, J., Drange, H., Fox-Kemper, B., Gleckler, P. J., Gregory, J. M., Haak, H., Hallberg, R. W., Heimbach, P., Hewitt, H. T., Holland, D. M., Ilyina, T., Jungclaus, J. H., Komuro, Y., Krasting, J. P., Large, W. G., Marsland, S. J., Masina, S., McDougall, T. J., Nurser, A. J. G., Orr, J. C., Pirani, A., Qiao, F. l., Stouffer, R. J., Taylor, K. E., Treguier, A. M., Tsujino, H., Uotila, P., Valdivieso, M., Wang, Q., Winton, M., and Yeager, S. G.: OMIP contribution to CMIP6: experimental and diagnostic protocol for the physical component of the Ocean Model Intercomparison Project, Geoscientific Model Development, 9, 3231–3296, https://doi.org/10.5194/gmd-9-3231-2016, 2016.

Guilyardi, E., Gualdi, S., Slingo, J., Navarra, A., Delecluse, P., Cole, J., Madec, G., Roberts, M., Latif, M., and Terray, L.: Representing El Niño in coupled ocean–atmosphere GCMs: The dominant role of the atmospheric component, Journal of Climate, 17, 4623–4629, https://doi.org/10.1175/JCLI-3260.1, 2004.

Guilyardi, E., Capotondi, A., Lengaigne, M., Thual, S., and Wittenberg, A. T.: ENSO modeling: History, progress, and challenges, in: El Niño Southern Oscillation in a Changing Climate, edited by: McPhaden, M. J., Santoso, A., and Cai, W., American Geophysical Union, American, 199-226, https://doi.org/10.1002/9781119548164.ch9, 2020.

Hallberg, R.: Using a resolution function to regulate parameterizations of oceanic mesoscale eddy effects, Ocean Modelling, 72, 92–103, https://doi.org/10.1016/j.ocemod.2013.08.007, 2013.

Harrison, D. E. and Vecchi, G. A.: Westerly wind events in the tropical Pacific, 1986–95*, Journal of Climate, 10, 3131–3156, https://doi.org/10.1175/1520-0442(1997)010<3131:Wweitt>2.0.Co;2, 1997.

He, B., Bao, Q., Wang, X. C., Zhou, L. J., Wu, X. F., Liu, Y. M., Wu, G. X., Chen, K. J., He, S. C., Hu, W. T., Li, J. D., Li, J. X., Nian, G. K., Wang, L., Yang, J., Zhang, M. H., and Zhang, X. Q.: CAS FGOALS-f3-L model datasets for CMIP6 historical atmospheric model intercomparison project simulation, Advances in Atmospheric Sciences, 36, 771–778, https://doi.org/10.1007/s00376-019-9027-8, 2019.

He, B., He, X. Y., Liu, Y. M., Wu, G. X., Bao, Q., Hu, W. T., Sheng, C., and Feng, S. J.: Role of thermal and dynamical subdaily perturbations over the Tibetan Plateau in 30-day extended-range forecast of East Asian precipitation in early summer, npj Climate and Atmospheric Science, 8, https://doi.org/10.1038/s41612-025-00931-2, 2025a.

He, X.-Y., He, B., Bao, Q., Liu, Y.-M., Li, J.-D., Wang, X.-C., Chen, X.-C., and Wu, G.-X.: The sensitivity of the Asian summer monsoon simulation to horizontal resolution and air−sea coupling in the FGOALS-f climate system model, Advances in Climate Change Research, 16, 44 – 57, https://doi.org/10.1016/j.accre.2025.01.008, 2025b.

Hersbach, H., Bell, B., Berrisford, P., Hirahara, S., Horányi, A., Muñoz-Sabater, J., Nicolas, J., Peubey, C., Radu, R., Schepers, D., Simmons, A., Soci, C., Abdalla, S., Abellan, X., Balsamo, G., Bechtold, P., Biavati, G., Bidlot, J., Bonavita, M., De Chiara, G., Dahlgren, P., Dee, D., Diamantakis, M., Dragani, R., Flemming, J., Forbes, R., Fuentes, M., Geer, A., Haimberger, L., Healy, S., Hogan, R. J., Hólm, E., Janisková, M., Keeley, S., Laloyaux, P., Lopez, P., Lupu, C., Radnoti, G., de Rosnay, P., Rozum, I., Vamborg, F., Villaume, S., and Thépaut, J. N.: The ERA5 global reanalysis, Quarterly Journal of the Royal Meteorological Society, 146, 1999–2049, https://doi.org/10.1002/qj.3803, 2020.

Hewitt, H. T., Roberts, M. J., Hyder, P., Graham, T., Rae, J., Belcher, S. E., Bourdallé-Badie, R., Copsey, D., Coward, A., Guiavarch, C., Harris, C., Hill, R., Hirschi, J. J. M., Madec, G., Mizielinski, M. S., Neininger, E., New, A. L., Rioual, J.-C., Sinha, B., Storkey, D., Shelly, A., Thorpe, L., and Wood, R. A.: The impact of resolving the Rossby radius at mid-latitudes in the ocean: results from a high-resolution version of the Met Office GC2 coupled model, Geoscientific Model Development, 9, 3655–3670, https://doi.org/10.5194/gmd-9-3655-2016, 2016.

Hua, L. J., Chen, L., Rong, X. Y., Su, J. Z., Wang, L., Li, T., and Yu, Y. Q.: Impact of atmospheric model resolution on simulation of ENSO feedback processes: a coupled model study, Climate Dynamics, 51, 3077–3092, https://doi.org/10.1007/s00382-017-4066-2, 2018.

Hunke, E. C. and Lipscomb, W. H.: CICE: The Los Alamos Sea Ice Model, Documentation and Software User's Manual, Version 4.1, Tech. Rep. LA-CC-06-012, Los Alamos National Laboratory, Los Alamos, New Mexico, available at: http://oceans11.lanl.gov/trac/CICE, 2010.

Jiang, W. P., Huang, P., Li, G., and Huang, G.: Emergent constraint on the frequency of central Pacific El Niño under global warming by the equatorial Pacific cold tongue bias in CMIP5/6 models, Geophysical Research Letters, 47, https://doi.org/10.1029/2020gl089519, 2020a.

Jiang, W. P., Huang, P., Huang, G., and Ying, J.: Origins of the excessive westward extension of ENSO SST simulated in CMIP5 and CMIP6 models, Journal of Climate, 34, 2839–2851, https://doi.org/10.1175/jcli-d-20-0551.1, 2021.

Jiang, X. N., Adames, Á. F., Kim, D., Maloney, E. D., Lin, H., Kim, H., Zhang, C. D., DeMott, C. A., and Klingaman, N. P.: Fifty years of research on the Madden-Julian Oscillation: Recent progress, challenges, and perspectives, Journal of Geophysical Research: Atmospheres, 125, https://doi.org/10.1029/2019jd030911, 2020b.

Jin, F.-F.: An equatorial ocean recharge paradigm for ENSO. Part I: Conceptual model, Journal of the Atmospheric Sciences, 54, 811–829, https://doi.org/10.1175/1520-0469(1997)054<0811:Aeorpf>2.0.Co;2, 1997.

Jin, F. F., Kim, S. T., and Bejarano, L.: A coupled-stability index for ENSO, Geophysical Research Letters, 33, https://doi.org/10.1029/2006gl027221, 2006.

Kim, S. T. and Jin, F.-F.: An ENSO stability analysis. Part II: Results from the twentieth and twenty-first century simulations of the CMIP3 models, Climate Dynamics, 36, 1609–1627, https://doi.org/10.1007/s00382-010-0872-5, 2011a.

Kim, S. T. and Jin, F.-F.: An ENSO stability analysis. Part I: results from a hybrid coupled model, Climate

Dynamics, 36, 1593–1607, https://doi.org/10.1007/s00382-010-0796-0, 2011b.

Kreussler, P., Caron, L. P., Wild, S., Loosveldt Tomas, S., Chauvin, F., Moine, M. P., Roberts, M. J., Ruprich-Robert, Y., Seddon, J., Valcke, S., Vannière, B., and Vidale, P. L.: Tropical cyclone integrated kinetic energy in an ensemble of HighResMIP simulations, Geophysical Research Letters, 48, https://doi.org/10.1029/2020gl090963, 2021.

Lawrence, D. M., Oleson, K. W., Flanner, M. G., Thornton, P. E., Swenson, S. C., Lawrence, P. J., Zeng, X., Yang, Z. L., Levis, S., and Sakaguchi, K.: Parameterization improvements and functional and structural advances in version 4 of the Community Land Model, Journal of Advances in Modeling Earth Systems, 3, https://doi.org/10.1029/2011MS00045, 2011.

Li, J., Yu, Y. Q., and Sun, D. Z.: Asymmetric Responses in the Equatorial Pacific to Wind Forcing in OMIP2 Experiments: Role of Zonal Currents, Geophysical Research Letters, 52, e2025GL114661, https://doi.org/10.1029/2025gl114661, 2025.

Li, J. X., Bao, Q., Liu, Y. M., Wang, L., Yang, J., Wu, G. X., Wu, X. F., He, B., Wang, X. C., Zhang, X. Q., Yang, Y. X., and Shen, Z. L.: Effect of horizontal resolution on the simulation of tropical cyclones in the Chinese Academy of Sciences FGOALS-f3 climate system model, Geoscientific Model Development, 14, 6113–6133, https://doi.org/10.5194/gmd-14-6113-2021, 2021.

Li, T.: Phase transition of the El Niño–Southern Oscillation: A stationary SST mode, Journal of the atmospheric sciences, 54, 2872–2887, https://doi.org/10.1175/1520-0469(1997)054<2872:PTOTEN>2.0.CO;2, 1997.

Li, T. Y., Yu, Y. Q., An, B., Luan, Y. H., and Chen, K. J.: Tropical instability waves in a high-resolution oceanic and coupled GCM, Ocean Modelling, 182, https://doi.org/10.1016/j.ocemod.2023.102169, 2023.

Li, Y., Liu, H., Ding, M., Lin, P., Yu, Z., Yu, Y., Meng, Y., Li, Y., Jian, X., and Jiang, J.: Eddy-resolving simulation of CAS-LICOM3 for phase 2 of the ocean model intercomparison project, Advances in Atmospheric Sciences, 37, 1067–1080, https://doi.org/10.1007/s00376-020-0057-z, 2020.

Liang, Y. and Fedorov, A. V.: Linking the Madden–Julian Oscillation, tropical cyclones and westerly wind bursts as part of El Niño development, Climate Dynamics, 57, 1039–1060, https://doi.org/10.1007/s00382-021-05757-1, 2021.

Liao, H. X., Cai, Z. C., Guo, J. S., and Song, Z. Y.: Effects of ITCZ poleward location bias on ENSO seasonal phase-locking simulation in climate models, Journal of Climate, 36, 5233–5249, https://doi.org/10.1175/jcli-d-22-0891.1, 2023.

Lu, B., Jin, F.-F., and Ren, H.-L.: A coupled dynamic index for ENSO periodicity, Journal of Climate, 31, 2361–2376, https://doi.org/10.1175/jcli-d-17-0466.1, 2018.

Lu, X. Q., Yu, H., Ying, M., Zhao, B. K., Zhang, S., Lin, L. M., Bai, L. N., and Wan, R. J.: Western north Pacific tropical cyclone database created by the China Meteorological Administration, Advances in Atmospheric Sciences, 38, 690–699, https://doi.org/https://10.1007/s00376-020-0211-7, 2021.

Ma, T., Yu, W.-D., Speich, S., Zhao, H.-K., Xin, R., Luo, H., and Wu, L.-G.: Philippine archipelago and South China Sea monsoon plus ocean cooling buffer Northwestern Pacific super typhoons, Nature Communications, 16, https://doi.org/10.1038/s41467-025-62334-4, 2025.

Madden, R. A. and Julian, P. R.: Detection of a 40–50 day oscillation in the zonal wind in the tropical Pacific, Journal of Atmospheric Sciences, 28, 702–708, https://doi.org/10.1175/1520-0469(1971)028%3C0702:DOADOI%3E2.0.CO;2, 1971.

Madden, R. A. and Julian, P. R.: Description of global-scale circulation cells in the tropics with a 40–50 day period, Journal of Atmospheric Sciences, 29, 1109–1123, https://doi.org/10.1175/1520-0469(1972)029%3C1109:DOGSCC%3E2.0.CO;2, 1972.

McPhaden, M. J., Zebiak, S. E., and Glantz, M. H.: ENSO as an integrating concept in earth science, Science, 314, 1740–1745, https://doi.org/10.1126/science.1132588, 2006.

Moore, A. M. and Kleeman, R.: Stochastic forcing of ENSO by the intraseasonal oscillation, Journal of Climate, 12, 1199–1220, https://doi.org/10.1175/1520-0442(1999)012<1199:Sfoebt>2.0.Co;2, 1999.

Nakamura, J., Camargo, S. J., Sobel, A. H., Henderson, N., Emanuel, K. A., Kumar, A., LaRow, T. E., Murakami, H., Roberts, M. J., Scoccimarro, E., Vidale, P. L., Wang, H., Wehner, M. F., and Zhao, M.: Western North Pacific Tropical Cyclone Model Tracks in Present and Future Climates, Journal of Geophysical Research: Atmospheres, 122, 9721–9744, https://doi.org/10.1002/2017jd027007, 2017.

Navarra, A., Gualdi, S., Masina, S., Behera, S., Luo, J. J., Masson, S., Guilyardi, E., Delecluse, P., and Yamagata, T.: Atmospheric horizontal resolution affects tropical climate variability in coupled models, Journal of Climate, 21, 730–750, https://doi.org/10.1175/2007jcli1406.1, 2008.

Planton, Y. Y., Guilyardi, E., Wittenberg, A. T., Lee, J., Gleckler, P. J., Bayr, T., McGregor, S., McPhaden, M. J., Power, S., Roehrig, R., Vialard, J., and Voldoire, A.: Evaluating climate models with the CLIVAR 2020 ENSO metrics package, Bulletin of the American Meteorological Society, 102, E193–E217, https://doi.org/10.1175/bams-d-19-0337.1, 2021.

Rayner, N. A., Parker, D. E., Horton, E. B., Folland, C. K., Alexander, L. V., Rowell, D. P., Kent, E. C., and Kaplan, A.: Global analyses of sea surface temperature, sea ice, and night marine air temperature since the late nineteenth century, Journal of Geophysical Research: Atmospheres, 108, https://doi.org/10.1029/2002jd002670, 2003.

Roberts, M. J., Camp, J., Seddon, J., Vidale, P. L., Hodges, K., Vanniere, B., Mecking, J., Haarsma, R., Bellucci, A., Scoccimarro, E., Caron, L.-P., Chauvin, F., Terray, L., Valcke, S., Moine, M.-P., Putrasahan, D., Roberts, C., Senan, R., Zarzycki, C., and Ullrich, P.: Impact of model resolution on tropical cyclone simulation using the HighResMIP–PRIMAVERA multimodel ensemble, Journal of Climate, 33, 2557–2583, https://doi.org/10.1175/jcli-d-19-0639.1, 2020a.

Roberts, M. J., Camp, J., Seddon, J., Vidale, P. L., Hodges, K., Vannière, B., Mecking, J., Haarsma, R., Bellucci, A., Scoccimarro, E., Caron, L. P., Chauvin, F., Terray, L., Valcke, S., Moine, M. P., Putrasahan, D., Roberts, C. D., Senan, R., Zarzycki, C., Ullrich, P., Yamada, Y., Mizuta, R., Kodama, C., Fu, D., Zhang, Q., Danabasoglu, G., Rosenbloom, N., Wang, H., and Wu, L.: Projected future changes in tropical cyclones using the CMIP6 HighResMIP multimodel ensemble, Geophysical Research Letters, 47, e2020GL088662, https://doi.org/10.1029/2020gl088662, 2020b.

Roberts, M. J., Reed, K. A., Bao, Q., Barsugli, J. J., Camargo, S. J., Caron, L.-P., Chang, P., Chen, C.-T., Christensen, H. M., Danabasoglu, G., Frenger, I., Fučkar, N. S., ul Hasson, S., Hewitt, H. T., Huang, H., Kim, D., Kodama, C., Lai, M., Leung, L.-Y. R., Mizuta, R., Nobre, P., Ortega, P., Paquin, D., Roberts, C. D., Scoccimarro, E., Seddon, J., Treguier, A. M., Tu, C.-Y., Ullrich, P. A., Vidale, P. L., Wehner, M. F., Zarzycki, C. M., Zhang, B., Zhang, W., and Zhao, M.: High-Resolution model intercomparison project phase 2 (HighResMIP2) towards CMIP7, Geoscientific Model Development, 18, 1307–1332, https://doi.org/10.5194/gmd-18-1307-2025, 2025.

Rong, X. Y., Zhang, R. H., Li, T., and Su, J. Z.: Upscale feedback of high-frequency winds to ENSO, Quarterly Journal of the Royal Meteorological Society, 137, 894–907, https://doi.org/10.1002/qj.804, 2011.

Savarin, A. and Chen, S. S.: Pathways to better prediction of the MJO:1. Effects of model resolution and moist physics on Atmospheric boundary layer and precipitation, Journal of Advances in Modeling Earth Systems, 14, e2021MS002928, https://doi.org/10.1029/2021ms002929, 2022.

Small, R. J., Bryan, F. O., Bishop, S. P., and Tomas, R. A.: Air–Sea turbulent heat fluxes in climate models and observational analyses: What drives their variability?, Journal of Climate, 32, 2397–2421, https://doi.org/10.1175/jcli-d-18-0576.1, 2019.

Song, M.: The code of FGOALS-f3 model study, Zenodo [code], https://doi.org/10.5281/zenodo.17778266, 2025.

Su, J. Z., Zhang, R. H., Li, T., Rong, X. Y., Kug, J. S., and Hong, C.-C.: Causes of the El Niño and La Niña amplitude asymmetry in the equatorial eastern Pacific, Journal of Climate, 23, 605–617, https://doi.org/10.1175/2009jcli2894.1, 2010.

Su, J. Z., Li, T., and Zhang, R. H.: The initiation and developing mechanisms of central Pacific El Niños, Journal of Climate, 27, 4473–4485, https://doi.org/10.1175/jcli-d-13-00640.1, 2014.

Sun, M., Li, T., and Chen, L.: El Niño phase-dependent high-frequency variability in western equatorial Pacific, Climate Dynamics, 55, 2165–2184, https://doi.org/10.1007/s00382-020-05376-2, 2020.

Tang, Y. L., HuangFu, J. l., Huang, R. H., and Chen, W.: Simulation and projection of tropical cyclone activities over the western North Pacific by CMIP6 HighResMIP, Climate Dynamics, 35, 7771–7794, https://doi.org/10.1175/JCLI-D-21-0760.1, 2022.

Thomson, D. J.: Spectrum estimation and harmonic analysis, Proceedings of the IEEE, 79, 1055-1096, https://doi.org/ 10.1109/PROC.1982.12433, 1982.

Timmermann, A., An, S. I., Kug, J. S., Jin, F. F., Cai, W., Capotondi, A., Cobb, K. M., Lengaigne, M., McPhaden, M. J., Stuecker, M. F., Stein, K., Wittenberg, A. T., Yun, K. S., Bayr, T., Chen, H. C., Chikamoto, Y., Dewitte, B., Dommenget, D., Grothe, P., Guilyardi, E., Ham, Y. G., Hayashi, M., Ineson, S., Kang, D., Kim, S., Kim, W., Lee, J. Y., Li, T., Luo, J. J., McGregor, S., Planton, Y., Power, S., Rashid, H., Ren, H. L., Santoso, A., Takahashi, K., Todd, A., Wang, G., Wang, G., Xie, R., Yang, W. H., Yeh, S. W., Yoon, J., Zeller, E., and Zhang, X.: El Nino-Southern Oscillation complexity, Nature, 559, 535–545, https://doi.org/10.1038/s41586-018-0252-6, 2018.

Yan, Y. and Sun, D.-Z.: Phase-Locking of El Niño and La Niña events in CMIP6 models, Atmosphere, 15, 882, https://doi.org/10.3390/atmos15080882, 2024.

Ying, J., Lian, T., Ren, H.-L., Zhang, C., Liu, T., and Tan, X.-X.: Effects of tropical cyclones on ENSO, Journal of Climate, 32, 6423–6443, https://doi.org/10.1175/jcli-d-18-0821.1, 2019.

Ying, M., Zhang, W., Yu, H., Lu, X. Q., Feng, J. X., Fan, Y. X., Zhu, Y. t., and Chen, D. Q.: An overview of the China Meteorological Administration tropical cyclone database, Journal of Atmospheric and Oceanic Technology, 31, 287–301, https://doi.org/https://10.1175/JTECH-D-12-00119.1, 2014.

Yu, Y. Q., An, B., Liu, H. L., Bao, Q., Lin, P. F., He, B., Zheng, W. P., Luan, Y. H., Bai, R. and Li, T. Y.: Review of the development and application of the high-resolution climate system model FGOALS, Chinese Journal of Atmospheric Sciences **(in Chinese**), 48, 200-217, https://doi.org/10.1007/BF02915571, 2024.

Yu, Y. Q., Tang, S. L., Liu, H. L., Lin, P. F., and Li, X. L.: Development and evaluation of the dynamic framework of an ocean general circulation model with arbitrary orthogonal curvilinear coordinate, Chinese Journal of Atmospheric Sciences **(in Chinese**), 42, 877–889, https://doi.org/10.3878/j.issn.1006-9895.1805.17284, 2018.

Zhang, R.-H., Yu, Y. Q., Song, Z. Y., Ren, H.-L., Tang, Y. M., Qiao, F. l., Wu, T. W., Gao, C., Hu, J. Y., Tian, F., Zhu, Y. C., Chen, L., Liu, H. L., Lin, P. F., Wu, F. H., and Wang, L.: A review of progress in coupled ocean-atmosphere model developments for ENSO studies in China, Journal of Oceanology and Limnology, 38, 930–961, https://doi.org/10.1007/s00343-020-0157-8, 2020.

Zhao, J. W., Wang, F., Zhan, R. F., Guo, Y. P., Huang, X., and Liu, C.: How Does Tropical Cyclone Genesis Frequency Respond to a Changing Climate?, Geophysical Research Letters, 50, https://doi.org/10.1029/2023gl102879, 2023.

Zhao, Y. D. and Sun, D.-Z.: ENSO asymmetry in CMIP6 models, Journal of Climate, 35, 5555–5572, https://doi.org/10.1175/jcli-d-21-0835.1, 2022.

Zhou, L., Bao, Q., Liu, Y. M., Wu, G. X., Wang, W. C., Wang, X. C., He, B., Yu, H. Y., and Li, J. D.: Global energy and water balance: Characteristics from F inite-volume A tmospheric M odel of the IAP/LASG (FAMIL 1), Journal of Advances in Modeling Earth Systems, 7, 1–20, https://doi.org/10.1002/2014MS000349, 2015.

Zi, P., Liu, Y. M., Li, J. D., Yang, R. W., He, B., and Bao, Q.: Reduced Spring Precipitation Bias and Associated Physical Causes over South China in FGOALS-f3 Climate Models: Experiments with the Horizontal Resolutions, Journal of Meteorological Research, 38, 784–804, https://doi.org/10.1007/s13351-024-3200-4, 2024.

Zuo, H., Balmaseda, M. A., Tietsche, S., Mogensen, K., and Mayer, M.: The ECMWF operational ensemble reanalysis–analysis system for ocean and sea ice: A description of the system and assessment, Ocean Science, 15, 779–808, https://doi.org/10.5194/os-15-779-2019, 2019.